

Organic & Biomolecular Chemistry

Accepted Manuscript



This is an *Accepted Manuscript*, which has been through the Royal Society of Chemistry peer review process and has been accepted for publication.

Accepted Manuscripts are published online shortly after acceptance, before technical editing, formatting and proof reading. Using this free service, authors can make their results available to the community, in citable form, before we publish the edited article. We will replace this *Accepted Manuscript* with the edited and formatted *Advance Article* as soon as it is available.

You can find more information about *Accepted Manuscripts* in the [Information for Authors](#).

Please note that technical editing may introduce minor changes to the text and/or graphics, which may alter content. The journal's standard [Terms & Conditions](#) and the [Ethical guidelines](#) still apply. In no event shall the Royal Society of Chemistry be held responsible for any errors or omissions in this *Accepted Manuscript* or any consequences arising from the use of any information it contains.

Artificial heme-enzyme with enhanced catalytic activity: evolution, functional screening and structural characterization.

Cite this: DOI: 10.1039/x0xx00000x

Received
Accepted

DOI: 10.1039/x0xx00000x

www.rsc.org/

Rosa Vitale,^a Liliana Lista,^a Corinne Cerrone,^a Giorgio Caserta,^b Marco Chino,^a Ornella Maglio,^{a,c} Flavia Natri,^a Vincenzo Pavone,^{*,a,d} Angela Lombardi^{*,a,d}

Synthetic proteins represent useful tools for reproducing metalloprotein functions in minimal, well-defined scaffolds. Herein, we describe the rational refinement of function into heme-protein models from Mimochrome family. Originally designed to mimic the *bis*-His cytochromes b, Mimochrome structure was modified to introduce a peroxidase-like activity, by creating a distal cavity on the heme. The success with the first asymmetric system, Mimochrome VI (MC6), gave the opportunity to explore further modifications in order to improve the catalytic activity. Starting from ferric MC6, single amino acid substitutions were introduced in the peptide chains to obtain four compounds, which were screened for peroxidase activity. The detailed structural and functional analysis of the best analogue, Fe^{III}-E²L(*TD*)-MC6, indicates that an arginine residue in proximity of the heme-distal site could assist catalysis by favoring the formation of the intermediate “compound I”, thus mimicking R³⁸ in HRP. This result highlights the potential of using small scaffolds for exploring the main factors that tune the heme-protein activity, and for programming new desired functions.

Introduction

Synthetic and engineered metalloenzymes represent powerful systems for understanding how metal cofactors and peptide scaffolds mutually influence their properties.^{1,2} Biomimetic metalloenzymes can embody key elements for accomplishing new or ordinary reactions,^{3–9} under conditions that are often incompatible with the reactivity of natural enzymes (*e.g.* in the presence of organic solvents, *etc.*).^{10,11}

Notably, in analyzing the differences between molecular evolution in nature and in laboratories, Pecoraro and colleagues have drawn the evolutionary process that allows nature to select, among several protein scaffolds, the best candidates with all requisites for a specific function. These include cofactors binding, chemo-, stereo- and regio-selectivity, *etc.*⁶ Progressively, it has been possible to develop bio-inspired functional molecules, and to move evolution from nature to laboratory. The effective power of protein design is constantly emerging and it has been possible to produce a considerable number of new reactive molecules and a number of their structures are populating data banks of biomolecules.^{12–15}

Our approach to artificial protein evolution has been directed on developing heme-protein mimetics (Mimochromes) by structure-based design. We have used a miniaturization process, aimed to reproduce the heme structural and

functional properties, even when embedded in small polypeptide scaffolds.

Mimochromes are peptide-deuteroporphyrin covalent conjugates, originally designed to reproduce the active site of globins and cytochromes.^{16,17}

Starting from the prototype, the symmetric *bis*-His 6-coordinated Mimochrome I,^{18–20} numerous compounds have been gradually produced in order to improve water solubility and to favor the formation of a unique and well-defined structure.^{21–24} Among the congeners of Mimochrome I, the catalytically active ferric derivative of Mimochrome VI (MC6), Fe^{III}-MC6, was designed to yield an asymmetric 5-coordinate complex. Fe^{III}-MC6 spectroscopic and functional characterization has showed its efficacy as biocatalyst, having the ability to perform a peroxidase-like catalytic activity towards 2,2'-azino-bis (3-ethylbenzthiazoline-6-sulphonic acid) (ABTS) and in the presence of the mild oxidant hydrogen peroxide.^{10,25,26} Interestingly, these studies have indicated that both peptide chains, covalently linked to the heme group, named tetradecapeptide (*TD*) and decapeptide (*D*), modulate MC6 properties. The mono-adduct, lacking the distal (*D*) chain, catalyzes ABTS oxidation with a higher *k*_{cat} respect to the whole structure Fe^{III}-MC6. This was interpreted in terms of a faster access of both H₂O₂ and ABTS to the iron site, when the (*D*) chain is missing. At the same time, Fe^{III}-MC6 mono-adduct shows also lower apparent affinity towards both substrates,

indicating that the (*D*) chain assists their binding. Finally, the quite high bleaching, as indicated by the much lower turnover number, suggests an important protective role of the (*D*) chain.¹⁰

The success of the initial design demonstrates that it is possible to incorporate a functional heme site within a minimal scaffold. Therefore, modification of the structure, through specific amino acid substitutions in the first and/or in the second coordination shell, should improve our understanding of the structure-activity relationship of Mimochromes.

The present study is aimed to improve the catalytic properties of MC6. Considering the ability of both peptides to finely tune the reactivity of MC6, our next step has now targeted the N- and C- terminal residues, Glu² and Arg¹⁰, in both (*D*) and (*TD*) chains. In MC6 design, these residues were supposed to stabilize both secondary and tertiary structures through electrostatic interactions (Fig.1).^{10,22} Therefore, we have replaced Glu² and Arg¹⁰ on both peptide chains with a hydrophobic Leu residue, to explore the role of charges on peroxidase activity. As a result of these substitutions, four analogues were obtained. Specifically, among these analogues, the most active compound, identified as E²L(*TD*)-MC6, has been subject to a detail structural and functional analysis.

The success in improving the reactivity of MC6 congeneric evolution demonstrates the usefulness of synthetic metalloproteins in delineating the role of individual amino acid in endowing particular functions.

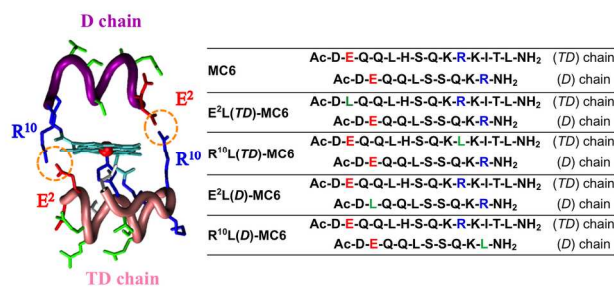


Fig. 1 Fe^{III}-MC6 and its analogues. (A) Molecular model of Fe^{III}-MC6 (generated with Visual Molecular Dynamics software, VMD: <http://www.ks.uiuc.edu/Research/vmd/>), highlighting the R¹⁰-E² ion pair interactions. (B) Peptide sequences of MC6 and its analogues: acidic, basic and non-polar residues, in position 2 and 10, are indicated in red, blue and green, respectively.

Results

Design and synthesis

The scaffold for our redesign was Fe^{III}-MC6, which is composed of a 14-residue peptide (*TD*) with a His at position 6, as fifth ligand to the heme (proximal face), and a ligand-free 10-residue peptide (*D*), apt to create a distal cavity around the heme (Fig. 1). As featured by all the members of the Mimochrome family, both peptide chains are covalently linked to the porphyrin propionates through the Lys⁹ side chains. The (*TD*) peptide chain was designed to adopt a short helical conformation (residues 1-9), a loop (residues 10-11), and a short β -strand (residues 12-14); the (*D*) peptide chain was designed in helical conformation. Unlike other Mimochromes, MC6

mimics the asymmetry of natural proteins in both primary and secondary coordination shells. This feature, together with the heme coordination state (5-coordinate, with a very weak sixth ligand) and the spin state (predominantly high spin), has been proven to be key factors for its peroxidase-like activity.

In order to verify the role in catalysis of E² and R¹⁰ charged residues of MC6, they were individually substituted in both the peptide chains with uncharged residue. These substitutions, however, were expected to partly destabilize the molecules, due to the consequent removal of inter-chain and/intra-chain interactions. To compensate this structure destabilization, leucine (L) was selected as substituting residue, because of its high α -helical propensity,^{21,28} and for the potential hydrophobic interaction with the porphyrin.¹⁹ Four Fe^{III}-MC6 analogues were obtained: E²L(*TD*), E²L(*D*) and R¹⁰L(*TD*), R¹⁰L(*D*).

All the peptide chains were synthesized by solid phase methodology, using 9-fluorenylmethoxycarbonyl (Fmoc) chemistry, and coupled to deuteroporphyrin in solution. After iron insertion by the acetate method,²⁹ slightly modified by us,¹⁸ the products were finally purified by reverse-phase HPLC and their identity was confirmed by LC-MS analysis. For more detailed description of protocols and synthetic results, please refer to supporting information (Fig. S1-S5, Table S1, ESI).

Functional screening

The catalytic properties of the Fe^{III}-MC6 analogues were explored to point out the effects of the amino acid substitution on function. A first screening for peroxidase-like activity was performed in the same experimental conditions previously used for Fe^{III}-MC6 (50 mM phosphate buffer pH 6.5, 50 % TFE, v/v, at 25 °C).¹⁰ A two-substrates Michaelis-Menten model (Eq. 1) was used to analyze the dependences towards ABTS and H₂O₂, and to determine the kinetic parameters (for details, please refer to ESI, Fig. S6-S9). Table 1 reports the catalytic parameters for all the analogues.

Table 1 MC6 and its analogues steady-state kinetic parameters. MC6 and HRP corresponding parameters are provided, for comparison. *Data from Thorneley *et al.*³⁰

Enzyme	pH	K _m (mM)		k _{cat} 10 ⁻² (s ⁻¹)	k _{cat} /K _m (mM ⁻¹ s ⁻¹)		T.O.N. 10 ⁻³
		H ₂ O ₂	ABTS (10 ⁻²)		H ₂ O ₂	ABTS (10 ⁻³)	
MC6	6.5	44 ± 2.0	8.4 ± 0.2	3.7 ± 0.1	8.4 ± 0.5	4.4 ± 0.2	4.0
E ² L(<i>TD</i>)-MC6	6.5	31 ± 2.0	5.0 ± 0.4	7.8 ± 0.6	25 ± 2.5	16 ± 0.2	5.9
R ¹⁰ L(<i>TD</i>)-MC6	6.5	54 ± 2.0	3.8 ± 0.1	6.8 ± 0.3	13 ± 0.7	18 ± 0.1	5.6
E ² L(<i>D</i>)-MC6	6.5	96 ± 7.0	11 ± 0.9	3.8 ± 0.3	4.0 ± 0.4	3.3 ± 0.4	3.6
R ¹⁰ L(<i>D</i>)-MC6	6.5	18 ± 1.0	3.0 ± 0.2	1.7 ± 0.1	8.6 ± 0.8	5.8 ± 0.5	3.3
HRP	4.6	0.85 ± 0.006	107 ± 1	62 ± 0.5	7.3 10 ³ ± 0.07	5.8 ± 0.07	50
HRP*	7.0	1.1 10 ⁻²	5.1	0.52	4.6 10 ³	0.01	0.3

When compared to MC6 catalytic properties, k_{cat} are about 2-fold higher in the analogues substituted at the (*TD*) chain. The best performances were obtained for E²L(*TD*)-MC6, which displays improvement in the apparent catalytic constant (k_{cat} = 7.8 · 10² s⁻¹), and efficiency for both H₂O₂ and ABTS (k_{cat}/K_m = 25 mM⁻¹ s⁻¹, and 16 · 10³ mM⁻¹ s⁻¹, respectively). In contrast, the analogues with the altered *D* chain showed an almost unmodified reactivity, respect to MC6. The E²L(*D*)-MC6 analogue was found to be the worst catalyst. Its k_{cat} is 3.8 · 10² s⁻¹, and the k_{cat}/K_m are 4.0 mM⁻¹ s⁻¹ for H₂O₂ and 3.3 · 10³ mM⁻¹ s⁻¹ for ABTS.

All MC6 analogues were able to perform several thousands of turnovers, without bleaching. The turnover numbers

(T.O.N.) reflects the trend of the catalytic efficiency, being higher in $E^2L(TD)$ -MC6 and lower in $R^{10}L(TD)$ -MC6. Based on its high catalytic performances, the $E^2L(TD)$ -MC6 analogue was selected for a more detailed structural and functional characterization. To gain more insight into the effects of the E^2L substitution in the (*TD*) chain on the catalytic properties, the influence of pH and 2,2,2-trifluoroethanol (TFE) were examined (Fig. 2). The pH profile of the initial rate (v_i) of the ABTS oxidation showed a bell-shaped curve, with a maximum at pH 6.5 (Fig. 2A). The v_i is also influenced by TFE, showing a pseudo-sigmoidal profile, with a maximum at 50 % TFE, in phosphate buffered solution pH 6.5 (Fig. 2B).

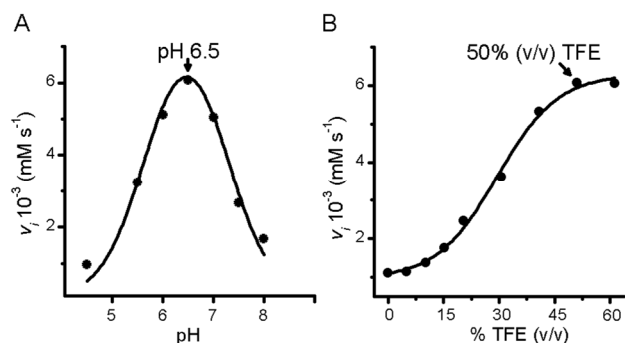


Fig. 2 Initial rate of ABTS oxidation as a function of pH (A) and TFE (B). Reaction conditions were: $T = 25^\circ\text{C}$, $E^2L(TD)$ -MC6 $2.0 \cdot 10^{-7}$ M, H_2O_2 3.0 mM, ABTS 0.1 mM, in (A) 50 mM phosphate solutions pH range 4.5–8.0 and (B) 50 mM phosphate buffer, pH 6.5, TFE range 0–60 % (v/v).

Spectroscopic characterization. UV-vis, circular dichroism (CD) and magnetic circular dichroism (MCD) spectroscopies were combined to gain information about the role of the pH and the TFE on the $E^2L(TD)$ -MC-6 properties.

Effects of pH. The coordination properties of $\text{Fe}^{\text{III}}\text{-}E^2L(TD)$ -MC6 were investigated by UV-vis pH titration, following the absorbance spectra modifications in the 2.0–10.0 pH range, in TFE/water solution (50 % v/v) (Fig. 3A, Table S2, ESI). The molar extinction coefficient (ϵ) at 387 nm was plotted as a function of pH. Data points were fitted to an equation describing the protonation state of three species involved in the pH-dependent equilibria (see Eq. 7, ESI). The best fit gave two transitions with midpoints at pH 2.8 (pK_{a1}), and 6.6 (pK_{a2}) (Fig. 3B).

At pH 2.0, the spectrum is typical of a mainly high spin (HS) *bis*-aquo ferric complex, exhibiting the Soret band at 386 nm, the Q bands at 495, 527 nm (shoulder, sh), and the CT (charge-transfer) band at 618 nm.

At pH 4.7, the lower intensity of the Soret (387 nm) and CT (616 nm) bands, together with their slight wavelength shifts, accounts for changes in the ferric ion axial coordination. These spectral features are consistent with a 6-coordinate species, predominantly in HS state, with a His- H_2O axial coordination. The effects of the ferric ion coordination justify the low apparent pK_a value (2.8) assigned to the His⁶ residue, as previously described for other artificial heme-proteins.^{10,11,22,31}

At pH 9.0, the Soret band further decreases in intensity and shifts to 388 nm, while the α (488 nm), β (517 nm, sh) and the CT (603 nm) bands move to higher energy. A

concomitant increase of the N band intensity at 342 nm (ratio to the Soret band up to 0.7) was also observed. The alkaline form of $E^2L(TD)$ -MC6 displays typical spectroscopic features of hydroxo-mimochrome complexes ($\text{His-Fe}^{\text{III}}\text{-OH}^-$), mostly in the HS state, with little contributions of the low-spin (LS) state.¹⁰

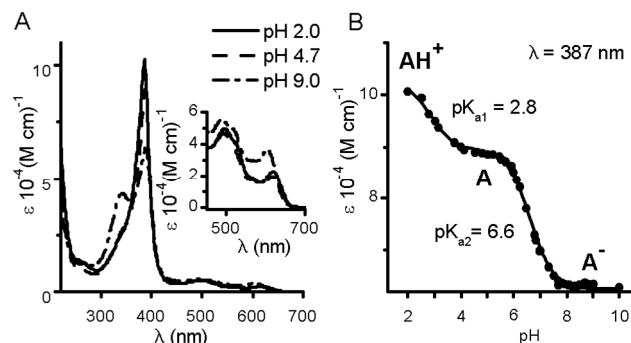


Fig. 3 UV-vis–pH titration of $\text{Fe}^{\text{III}}\text{-}E^2L(TD)$ -MC6 ($7.0 \cdot 10^{-6}$ M) in H_2O /TFE solution (50 % v/v). (A) pH dependence of the Soret and visible-region (inset) spectra. (B) Plot of the Soret molar extinction coefficient (ϵ , at 387 nm) as a function of pH. Data points were fitted according to equation 7 (ESI). $T = 25^\circ\text{C}$.

To better characterize the heme coordination states, magnetic circular dichroism spectra (MCD) were collected at three different pHs (Fig. 4, Table S3 ESI).

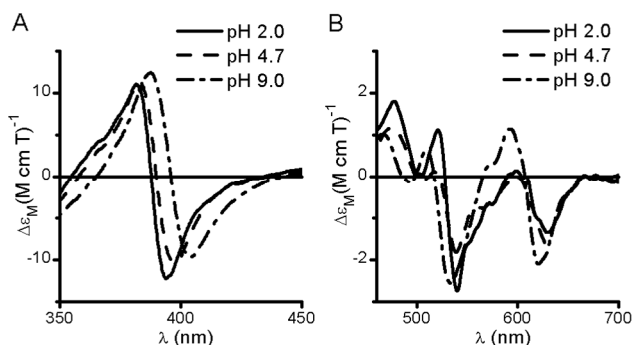


Fig. 4 $\text{Fe}^{\text{III}}\text{-}E^2L(TD)$ -MC6 MCD spectra. (A) Soret and (B) visible regions. Experimental conditions: $\text{Fe}^{\text{III}}\text{-}E^2L(TD)$ -MC6 ($2.0 \cdot 10^{-5}$ M), in 50 mM phosphate solutions at different pH, 50 % TFE (v/v), $T = 25^\circ\text{C}$.

In the Soret region, all the MCD spectra of $\text{Fe}^{\text{III}}\text{-}E^2L(TD)$ -MC6 have similar S-shape and intensity (Fig. 4A). At pH 2.0, the spectrum shows a maximum at 381 nm, a shoulder at 365 nm and a trough at 394 nm, with a crossover at 387 nm. At pH 4.7, the spectrum is quite similar, with slightly red-shifted peak (383 nm), trough (398 nm) and crossover (390 nm). The spectrum obtained at pH 9.0 is significantly modified and all the bands move to higher wavelength: the maximum is detected at 387 nm, the λ_0 at 396 nm and the trough at 404 nm.

In the visible region, MCD spectra show sinusoidal-like curves, mainly linked to Q (~ 500 nm) and the CT (~ 600 nm) bands (Fig. 4B). At pH 2.0, two maxima are detected at 478 and 520 nm, a main trough falls at 540 and a weaker one at 630 nm. At pH 4.7 the main differences are in the Q band region, where only the maximum at 478 nm is clearly observed. At higher wavelength the bands position remains unchanged, but the 540 nm/630 nm ratio is halved respect to the acidic species at pH 2.0. At pH 9.0, the Q bands are detected at 466 and 508 nm, as two maxima, two

troughs at 535 and 620 nm are also detected, and a peak at 590 nm, with a shoulder 570 nm, appears.

The red shift of the Soret band and the blue shift of the visible bands at increasing pHs describe a HS-LS equilibrium, which progressively shifted towards LS as the pH increases. However, according to Vikery *et al.*^{32,33}, the complexity of the visible band region suggests that the ligand exchange leaves the spin state reasonably closer to the HS.

Effects of TFE. CD spectroscopy was used to analyze the effects of TFE on Fe^{III}-E²L(TD)-MC6 structure (Fig. 5 and 6). TFE titration was performed in the 0-50 % (v/v) range, in 50 mM phosphate solution. The pH was set at 4.7, where the His-H₂O was the predominant species.

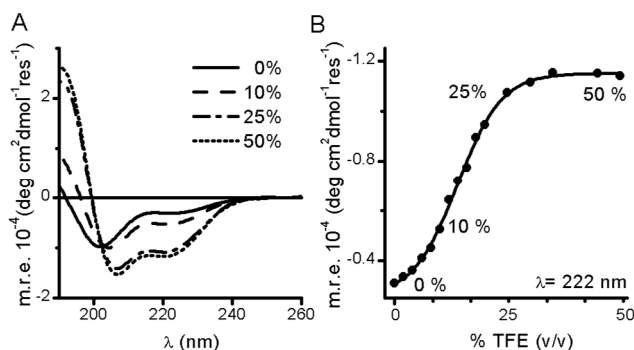


Fig. 5 Far-UV region CD spectra of Fe^{III}-E²L(TD)-MC6 (2.0·10⁻⁵ M) in 50 mM phosphate solutions (pH 4.7). (A) Spectra at different TFE concentrations. (B) Titration curve showing θ_{222} as function of TFE concentration (% v/v). T = 25 °C.

Two negative bands, around 220-222 nm (amide transition $n-\pi^*$) and 200-207 nm (amide transition $\pi-\pi^*$), and a positive band around 190 nm (amide transition $\pi-\pi^*$, perpendicular coupling) characterize all the far-UV spectra (Fig. 5A).

In the absence of TFE, the CD spectrum shape and intensity describe the peptide chains as poorly structured and mainly in random-coil conformation. Upon TFE addition, the mean residue molar ellipticity at 222 nm (θ_{222}) increases, the θ_{ratio} ($\theta_{222}/\theta_{min}$) value progressively becomes closer to the unity, the λ_{min} shifts towards 207 nm, and the λ_0 shifts to higher wavelengths. All these features are indicative of a stabilization of an α -helical structures (Fig. 5, Tab. S4, ESI). The plot of the θ_{222} as function of TFE shows a sigmoidal increase of the secondary structure content, reaching the helical stabilization at 30 % TFE (v/v), and the maximum value at 50 % TFE (v/v), where no more structural transitions are observed (Fig. 5 B).

In order to elucidate the peptide-deuteroheme interactions in the TFE-dependent sandwiched structure, the induced Cotton effects (C.E.) in the Soret region were also examined (Fig. 6, Table S5, ESI). At low TFE concentrations (< 20 % v/v), weak negative peaks, centered at 386 nm, depict the CD spectra. By increasing the TFE concentration, the Cotton effect progressively intensifies ($\theta_{386} = 1.51 \cdot 10^4$ deg cm² dmol⁻¹ at 50 % v/v TFE), and peaks becomes well resolved (Fig. 6A). Analogously, the plot of θ_{386} as function of TFE percentage shows a sigmoidal increase of the induced C.E., that reaches a plateau at 50 % TFE (v/v) (Fig. 6 B). The spectroscopic features of E²L(TD)-MC6 were also investigated in the conditions of maximum catalytic activity (pH 6.5, in the presence of 50 % TFE) (Fig. 7, Table S2-S5, ESI).

The far-UV CD spectrum demonstrated that the secondary structure content at pH 4.7 and 6.5 are almost identical. However, all the other spectroscopic properties are intermediate between

those at pH 4.7 (His-H₂O axial ligation) and at pH 9.0 (His-OH⁻ species). The C.E. in the Soret CD spectrum (θ_{386} of $1.0 \cdot 10^4$ deg cm² dmol⁻¹), weaker than that obtained at pH 4.7, is related to the almost 50 % presence of the His-OH⁻ complex, according to the UV-vis pH titration (Fig. 3). In the UV-vis absorption spectrum the Soret band is found at 387 nm ($\epsilon = 68 \cdot 10^3$ M⁻¹ cm⁻¹), the α band at 489 nm, the β band at 518 nm (sh) and the CT band at 610 nm. The Soret MCD band shows a maximum at 385 nm, the λ_0 at 393 nm and the trough at 403 nm. In the visible Q region, bands are detected at 470 and 508 nm as two peaks; two troughs at 538 and 627 nm are detected, and a peak at 590 nm, with a shoulder 570 nm.

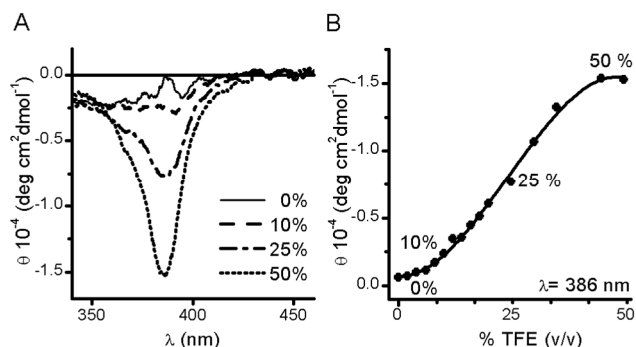


Fig. 6 Soret region CD spectra of Fe^{III}-E²L(TD)-MC6 (2.0·10⁻⁵ M) in 50 mM phosphate buffered solutions (pH 4.7). (A) Spectra at different TFE concentrations. (B) Titration curve, showing θ_{386} as function of TFE concentration (% v/v). T = 25 °C.

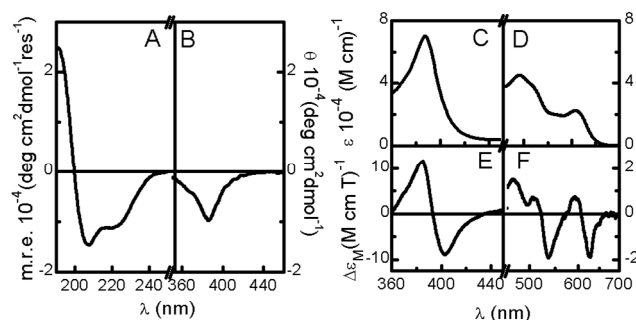


Fig. 7 Spectral properties of Fe^{III}-E²L(TD)-MC6 (2.0·10⁻⁵ M) in 50 mM phosphate buffered solutions (pH 6.5) / TFE (50 %, v/v), T = 25 °C. (A) and (B): CD spectra in the far-UV and Soret region, respectively. (C) and (D): UV-vis absorption spectra in the Soret and visible region, respectively. (E) and (F): MCD spectra in the Soret and visible region, respectively.

Discussion

Leucine scanning was successfully used to explore the Fe^{III}-MC6 structure/function relationships, and to select new mimetics with improved catalytic properties (Fig. 8).

The functional characterization demonstrates that all the analogues retained a peroxidase-like catalytic activity, with high stability in turnover conditions. This result confirmed the correctness of the design of asymmetric mimochromes for catalytic purposes. Further, it highlights that a structural simple scaffold is well suited for amino acid substitutions, without losing the catalytic activity.

The four leucine-substituted analogues showed different site-dependent catalytic efficiencies (Fig. 8, 9), thus confirming their suitability for structure-function relationship analysis.

The observed differences in the catalytic efficiencies upon R¹⁰L or E²L substitutions are not simply related to heme environment modifications, which result from the replacement of charged with hydrophobic amino acids. Such differences seem to be more strictly related to the peptide chain (*TD* or *D*) where the substitution occurs. Surprisingly, E²L and R¹⁰L substitutions in (*TD*) chain bettered the catalytic efficiencies of both substrates H₂O₂ and ABTS. Conversely, E²L and R¹⁰L substitutions in the (*D*) chain worsened the catalytic efficiencies (Fig. 8).

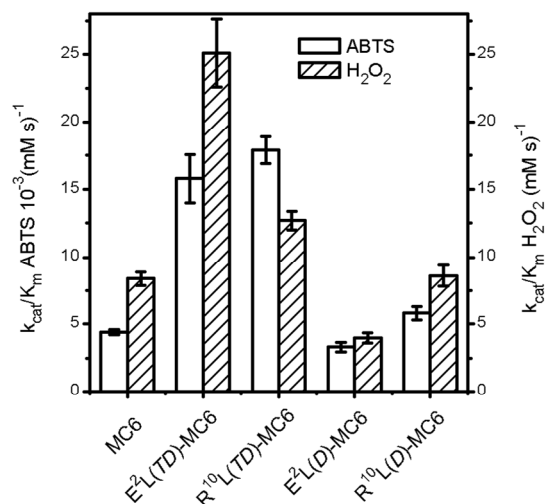


Fig. 8 Catalytic efficiencies ($k_{\text{cat}}/K_{\text{m}}$) towards ABTS (empty bars) and H₂O₂ (dashed bars) in the peroxidation reaction catalyzed by MC6 and its analogues (kinetic parameters from Tab.1). Error bars are reported.

By taking advantage of the NMR solution structure of Co^{III}-Mimochrome IV,²² we could evaluate the effect of Leu shuffling on the overall structure of MC6, with respect to the electrostatic charged Glu and Arg residues (Fig. 9). In fact, Arg and Glu residues in Co^{III}-Mimochrome IV form inter-chain ion pairing interactions.

With the aim of determining the beneficial effect of the catalyst from bleaching, two factors were taken into account: (i) direct involvement of distal E² and/or R¹⁰ on k_{cat} (see Fig. 9 B, C); (ii) indirect effect of E² and/or R¹⁰, in stabilizing the sandwich structure (see Fig. 9 A-E).

The role of E² in (*D*) chain. The E² residue in the (*D*) chain was found to be essential for catalysis, since the E²L(*D*) substitution considerably drops the catalytic efficiencies (Fig. 8). The role of this residue can be explained considering the pH-dependent reactivity of E²L(*TD*)-MC6 (Fig. 2A), and of the parent compound MC6.¹⁰ In both cases, data fitting of the v_i vs. pH, according to model equation described elsewhere,¹⁰ gave a $\text{p}K_{\text{a}1} \approx 5$ and a $\text{p}K_{\text{a}2} \approx 7$, with the maximum activity at pH 6.5. This indicates that at least two ionizable groups are involved in the modulation of the reactivity. The first transition can be attributed to the deprotonation of the E² in the (*D*) chain, which thus could ion-pair with the R¹⁰ on the (*TD*) chain (Fig. 9 A, B, E). Based on this interpretation, it is possible to conclude that this ionic interaction positively modulates the structural and catalytic properties of the mini-enzyme, stabilizing the sandwich structure, and protecting the catalyst from bleaching.

When the pH exceeds the value of 7, the harder hydroxide coordination (see Fig. 3 and 10) interferes with the H₂O₂ binding and catalysis triggering, causing decrease in efficiency.

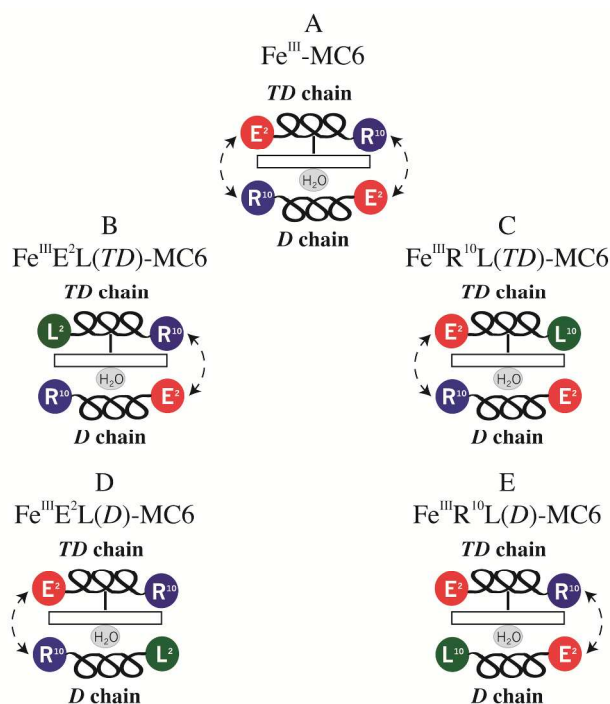


Fig. 9 Hypothetical schematic models describing the possible intra-chain ion pairing (broken arrows) for MC6 and its Leu containing analogues.

The role of R¹⁰ in (*D*) chain. The R¹⁰ residue in the decapeptide chain could contribute to improve the catalytic performances, when not involved in any other interaction. In fact, MC6 (where R¹⁰ is engaged in ion-pair, Fig. 9 A) and the R¹⁰L(*D*) analogue (where R¹⁰ is absent, Fig. 9 E) show similar catalytic efficiencies (Fig. 8).

The beneficial effect of the free R¹⁰ in (*D*) chain is supported by the spectroscopic data from the UV-vis (Fig. 3, 7), MCD (Fig. 4, 7), and CD (Fig. 5-7) characterization on E²L(*TD*) analogue. The overall data seem to indicate a different structural arrangement of the heme environment, respect to MC6.

UV-vis pH titration data were used to describe the three pH-dependent species (Fig. 10). At acidic pH (2.0), the HS/*bis-aquo* species, called AH⁺, is predominant. A second species, called A, is also present at about 20 %, reaching the maximum concentration at pH 4.7. It corresponds to a predominantly HS deuteroheme, with His-H₂O axial ligands. Starting from pH 5.7, the A⁻ species appears, in which the harder hydroxide ligand, in place of the water molecule, binds the ferric ion, thus providing little contribution of LS state.

The overall shapes and band shifts of the MCD spectra, both in the Soret and visible region, reflect the trend observed by UV-vis spectroscopy, related to the ligand exchange equilibria (Fig. 4).

It has been observed that, in heme-proteins and in heme complexes, the position, the complexity and the relative intensity of the MCD bands can be related to HS/LS amount, which is typically influenced by the sixth axial ligand.³²⁻³⁴ Comparisons with Cyt *c*,³² met-Mb,³³ ferric-HRP^{35,36} and Fe^{III}-MP3,¹¹ a heme-protein model designed by miniaturizing the Bacterioferritin active site, supports the E²L(*TD*)-MC6 pH-

dependent coordination state. All these molecules have a proximal histidine as heme^{33,35,36} or deuteroheme¹¹ ligand.

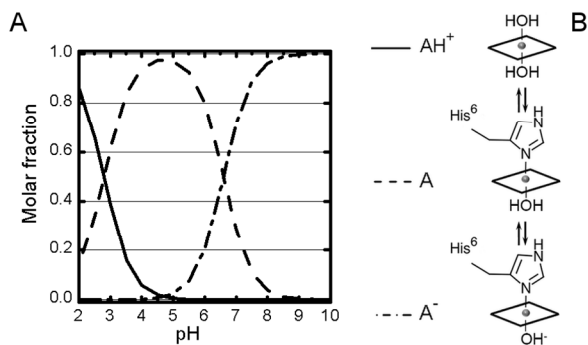


Fig. 10 (A) Proposed pH equilibria and species involved. (B) Speciation curves as a function of pH (data from UV-vis pH titration in Fig. 3).

MCD spectra of E²L(TD)-MC6 are quite similar to those reported for MP3, apart from some minor differences at acidic pH, where MP3 presents a higher HS contribution. In both cases, the spectra of the alkaline species are closer to the predominantly HS Mb-hydroxide,³³ respect to the LS HRP-hydroxide.³⁶ Although OH⁻ is a stronger ligand than water, it appears to be not strong enough to make the LS state the predominant one at room temperature.

The complex visible region of the MCD spectra further confirms the almost pH-independent HS state of E²L(TD)-MC6. The CT band above 600 nm, at all the examined pH, is characteristic of high spin and it is also influenced by the degree of hydrogen-bonding interactions, between the distal environment and the sixth ligand.¹¹ MP3 CT band, located at 627 nm, was assumed to be consistent with a weak hydrogen bond, between Arg¹³ (on the heme distal site) and the OH⁻. This weak hydrogen bond decreases the OH⁻ to Fe^{III} charge donation, causing a CT redshift in the MCD spectrum, if compared with metMb (CT at 620 nm), where no direct hydrogen bonds involve the hydroxide ligand.

E²L(TD)-MC6 MCD spectra showed a similar CT band, at 629 nm at pH 2.0 and 4.7, and at 627 nm at pH 6.5, suggesting that the distal Arg¹⁰ might interact with an H-bond acceptor in the sixth coordination position. At higher pH (9.0), the deprotonation of its guanidine group could cause this H-bond destabilization, thus justifying the CT at 620 nm of the E²L(TD)-MC6 alkaline form. This quite surprising pK_a value of Arg side chain was already reported for Mimochrome IV.²²

All together, these spectroscopic data support the involvement of Arg¹⁰ in helping substrate binding in the distal pocket.

The role of pH on the E²L(TD)-MC6 sandwiched structure.

Far-UV CD spectroscopy showed negligible effects of the pH on the α -helix content, thus demonstrating that the almost complete induction of peptides secondary structure is related to TFE content (see Fig. 5A and 7A).

Soret CD spectra were suitable to investigate the role of pH in stabilizing the sandwiched structure.

Coupling of π - π^* heme transition with π - π^* and n - π^* transitions localized in the polypeptide backbone, or with π - π^* transitions of aromatic side chains is considered to be the main factor that induce C.E. in hemoproteins.^{18,37,38}

In the case of small heme-peptide systems, lacking aromatic residues, as E²L(TD)-MC6, coupling of the heme with the peptide backbone transitions and with the coordinating His accounts for the observed Soret C.E.^{28,29}

The asymmetric E²L(TD)-MC6 displayed a Soret C.E., which is significantly affected by pH. At acidic pH (2.0, 50 % TFE) no

induced C.E. is detected, probably because the peptide chains are fluctuating around the deuteroheme plane, and the peptide-porphyrin interactions in the H₂O-Fe^{III}-H₂O coordination state are very weak (data not shown). By increasing the pH, the progressively deprotonated His⁶ coordinates the ferric ion, thus drawing the (TD) chain closer to the deuteroheme, and stabilizing the sandwiched structure. A further contribution is given by the E²(D) deprotonation at pH around 5, as highlighted in the previous paragraph. The lower C.E. observed at higher pH, e.g. 6.5 (compare Fig. 6 and 7, Table S5, ESI), could be explained by the increasing hydroxide-Fe^{III} coordination, which provides a small LS contribution. In fact, CD spectra intensities, in the Soret region, are influenced by the spin moment: generally the higher HS amount is, the larger CD intensity is observed.³⁹

The relation between TFE-dependent sandwiched structure and activity.

Figure 2B reports the positive effects of TFE concentration on the catalytic performances. Fluorine substituted alcohols, such TFE, are well known in peptide chemistry for their marked potential to induce and stabilize secondary structure, e.g. α -helices.⁴⁰⁻⁴⁵

TFE may act in different ways, by weakening hydrophobic interactions, strengthening intramolecular hydrogen bonds, changing the dielectric constant of the solvent and acting as an osmolyte. However, up to the date there is no unique model describing the mechanism of induced folding.

X-ray scattering demonstrated that fluorinated alcohols form micelle-like clusters in water, whose dimensions seem to be influenced by alcohol percentage and local concentration.^{43,44}

Based on the ability of TFE to interact with water molecules, Reiersen and Rees proposed a “push and pull” mechanism to explain the TFE-assisted folding.⁴⁴ The “pull phase” acts at lower TFE concentration (0-10 %), where clusters are not fully stabilized and water molecules surround the surface of amino acid side chains. When clusters become larger and more compact (until 50 %), TFE molecules could directly interact with hydrophobic side chains, thus providing a matrix assisted driving force for folding (push phase). This kind of matrix is important to lower the side chain conformational entropy and, hence, facilitate peptides folding. Roccatano *et al.* used MD simulations to study the effect of TFE as a water-cosolvent on peptides stability.³⁵ Their simulations confirmed that TFE clusters assist the folding, by promoting the formation of local peptide interactions and, as a consequence, of ordered secondary structure.

All Mimochromes, showed their peptide secondary structure strictly related to the presence of TFE as cosolvent.^{10,18,19,23} In particular, for MC6, TFE-dependent peptide structures were nicely correlated to the catalytic performances, thus demonstrating that the correct folding of both chains is necessary for reactivity.¹⁰

Far-UV CD demonstrated that E²L(TD)-MC6 α -helix content increases in the presence of TFE. The unfolded \leftrightarrow folded transition occurs at about 10 % TFE (possible pull phase) and the helix stabilization is reached in 30-50 % TFE range (possible push phase) (Fig. 5). Fig. 6 shows that the Soret C.E. ($\lambda = 386$ nm) also increases at increasing TFE content, suggesting that the stabilization of the secondary structures facilitates inter-chains and peptide-heme interactions. This mutual correlation between the secondary and the tertiary structures, related to TFE content, is clearly represented in Fig. 11.

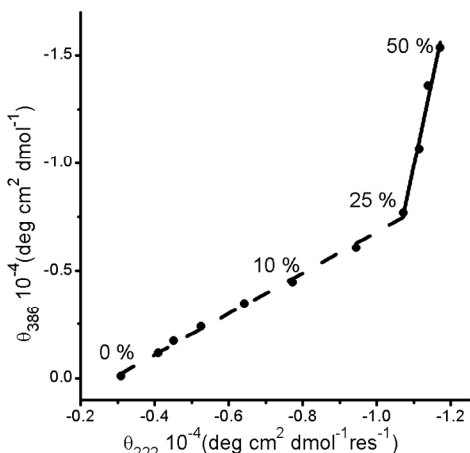


Fig. 11 Plot of θ_{386} vs. θ_{222} at different TFE concentrations (% v/v). θ_{386} is reported as total ellipticity, while θ_{222} as mean residue ellipticity. Tags are referred to 0, 10, 25 and 50 % (v/v), respectively.

Two linear fits, with different slopes, are observed in the 0-25 % and 25-50 % TFE regions. By assuming that the induced C.E. may result from a coupling of the heme (π - π^*) and the peptide chain backbone (π - π^* and n - π^*) transitions, we propose that the progressively intensified C.E.s, up to 25 % TFE, are correlated to the random coil \leftrightarrow helix transition. In fact, the little induced C.E., at low TFE content, can be explained as the sum of the contributions of different and poorly organized peptide structures. At higher TFE concentrations (up to 50 %), once reached the predominant α -helical species, the well-defined induced C.E. describes an almost unique sandwiched structure, which displays the highest reactivity. Our experimental evidences prove the role played by TFE clusters in peptide folding, and confirm the effectiveness of the “push and pull” theory also for more complex systems.

Conclusions

This work was focused on the rational design, synthesis, and characterization of heme-protein mimetics with peroxidase-like catalytic activity. The molecular scaffold of the parent Fe^{III}-MC6 was used to introduce point substitutions in the peptide sequences to extend their structural and functional variability. The functional screening has allowed to select Fe^{III}-E²L(TD)-MC6 as the best compound, in terms of catalytic efficiencies and turnover number. While being more than tenfold smaller in terms of molecular weight, Fe^{III}-E²L(TD)-MC6 has improved enzyme-like properties, that in turn approach HRP.

Importantly, Fe^{III}-E²L(TD)-MC6 displays the maximal activity at about neutral pH (6.5), as in comparison to HRP. This represents an important outcome, since this synthetic enzyme is able to efficiently catalyze reactions that require high pH conditions (e.g. tyrosine coupling, data not shown). It should be outlined that at pH 6.5 the catalytically active His-H₂O species is not predominant (molar fraction 0.5, see Fig. 9). Considering that E²L(TD)-MC6 lacks a residue in the active site able to assist hydrogen peroxide deprotonation similarly to His⁴² in HRP,⁴⁶⁻⁴⁹ pH 6.5 may represent a compromise, which simultaneously ensures the highest amount of His-H₂O coordination state and hydrogen peroxide deprotonation and binding to the Fe^{III} resting state.

UV-vis, CD and MCD spectroscopies were combined to get insight into the molecular basis of the catalytic improvement, correlating the primary, secondary and tertiary structures of the

mini-enzyme with the spin state of the metal ion and the nature of the axial ligands.

Based on the E²L(TD)-MC6 model, it is possible to hypothesize a catalytic role of R¹⁰ on the (D) chain. Its side chain may approach the ferric ion and interact, by hydrogen bond, with the sixth ligand to the heme. Hence, R¹⁰ is supposed to mimic R³⁸ in HRP distal site and to enhance the efficiency of the compound I formation and the ligand binding.^{30,47,50}

Further, spectroscopic analysis evidences that the Fe^{III}-E²L(TD)-MC6 catalytic cycle occurs with a peroxidase-like mechanism, through the formation of compound I, containing a Fe^{IV}=O center and a porphyrin radical cation (for details see Fig. S10, ESI).

This preliminary mechanistic results further confirms E²L(TD)-MC6 similarities with natural peroxidases, whose reactivity is influenced by the proximal and distal heme environments.

Collectively, the experimental results allow to point out the principle in heme-protein reactivity: slight structural modifications in the heme-distal pocket may greatly influence the peroxidase-like activity.

Moreover, the characterization of this class of mini-enzymes demonstrates that their miniaturized structure holds essential elements to finely tune reactivity. This represents a very important checkpoint for the rational design of new and improved biomimetic catalysts, tailored to specific applications. Further design, based on the results herein reported, will be aimed to (i) stabilize both the helical and the sandwiched structures by introducing additional structural constraints; (ii) favor the His-H₂O species over a wider pH range; (iii) introduce amino acid residues assisting the acid-base catalytic cleavage of the O-O bond, as His⁴² acts in HRP.⁴⁶⁻⁴⁹

Materials and methods

Catalytic assays: ABTS oxidation causes the formation of a radical cation product, which is easily detectable by spectrophotometric measurements (ABTS^{•+} λ_{\max} = 660 nm; ϵ = $1.40 \cdot 10^4$ M⁻¹ cm⁻¹). The catalytic experiments were followed measuring the appearance of the reaction product, by a Varian Cary 50 spectrophotometer. ABTS stock solutions were prepared in phosphate buffer (50 mM, pH 6.5) and their concentrations were assessed spectrophotometrically (λ_{\max} = 340 nm; ϵ = $3.66 \cdot 10^4$ M⁻¹ cm⁻¹). H₂O₂ stock solutions were prepared by diluting H₂O₂ (30 % v/v) in water, whose concentration was determined by UV-vis absorption spectroscopy (λ_{\max} = 240 nm; ϵ = 39.4 M⁻¹ cm⁻¹).

Fe^{III}-MC6 analogues stock solutions were prepared in acidic water (0.1 % TFA, v/v, pH = 1.8) and diluted in 660 μ L of phosphate buffer (50 mM, pH 6.5, 50 % v/v TFE). The progress curves of the reaction were monitored at λ_{\max} = 660 nm, with an average time of 0.1 sec, under mild magnetic stirring and at T = 25 °C.

The (TD)-substituted analogues concentration was at $2.0 \cdot 10^{-8}$ M.

For the analysis of the dependence towards the oxidizing substrate, ABTS concentration was fixed ($1.0 \cdot 10^{-1}$ M), while different H₂O₂ concentration, in the range of $1.0 \cdot 10^{-4}$ - $2.0 \cdot 10^{-2}$ M were explored. When studying the dependence towards the reducing substrate, H₂O₂ concentration was fixed, $2.0 \cdot 10^{-2}$ M for E²L(TD) and $1.0 \cdot 10^{-2}$ M for R¹⁰L(TD), while ABTS was varied, $5.0 \cdot 10^{-6}$ - $1.0 \cdot 10^{-4}$ M.

The concentration of the (D)-substituted catalyst was fixed at $2.0 \cdot 10^{-7}$ M, because of their lower catalytic activity. Experiments were carried out (i) at steady ABTS ($1.0 \cdot 10^{-1}$ M) and variable H₂O₂ concentrations ($1.0 \cdot 10^{-4}$ - $2.0 \cdot 10^{-2}$ M) and, *vice versa*, (ii) at constant H₂O₂ (50 mM for M6 E²L(D), 20 mM for R¹⁰L(D)) and

different ABTS concentrations ($5.0 \cdot 10^{-6}$ – $1.0 \cdot 10^{-4}$ M). Temperature was set at 25 °C and the reaction mixture was stirred magnetically. In all catalytic analysis, 1 cm path length quartz cuvettes were used.

K_m and k_{cat} values were determined by using a two-substrate Michaelis–Menten kinetic model. Data were analyzed by using equation (1) in which v is the initial rate, $[E]_0$ is the enzyme concentration, $[A]$ is the H_2O_2 concentration, and $[B]$ is the substrate concentration.

$$v = \frac{k_{cat}[E]_0}{1 + \frac{K_A}{[A]} + \frac{K_B}{[B]}} \quad (\text{eq. 1})$$

UV-vis absorbance, CD and MCD characterization. The pH-titration experiments were carried out, by diluting ferric $E^2L(TD)$ -MC6 to $7.0 \cdot 10^{-7}$ M final concentrations, in H_2O and TFE (50 % v/v). The UV-vis absorption spectra were recorded in 1 cm path length quartz cuvettes. Wavelength scans were performed in the 200–800 nm range, with a 300 nm/min scan rate, 2.0 nm data interval and an average time of 0.0125 s, with the temperature set at 25 °C. NaOH (0.1 M) was used for the basic titration, whereas solutions of TFA (0.1, 1 and 10 % v/v in water, or 100 %) were used in the acidic titration (dilution was less than 1 % and considered in the final data). A lab pH meter (pHM220, Meterlab-Radiometer analytical) was used to assess the pH. It was equipped with a biotrode electrode (Hamilton), and calibrated in the 1.679–10.012 pH range by using IUPAC standard solutions (Radiometer analytical).

CD and MCD experiments were performed on a Jasco J-815 circular dichroism spectropolarimeter, calibrated for intensity with ammonium $[D_{10}]$ camphorsulfonate ($[\theta]_{290,5} = 7910 \text{ deg cm}^2 \text{ dmol}^{-1}$). Depending on the observed region, the cell path length was 0.1 or 1.0 cm. CD spectra were recorded in the 290–260 nm (far-UV) and 460–340 nm (Soret) regions, at 0.2 nm intervals, with a 20 nm/min scan rate, 1.0 nm bandwidth and a 16 s response. In order to improve the signal to noise ratio 3 and 5 accumulations were collected for the far-UV and Soret- regions, respectively. Spectra are reported in terms of mean residue ellipticity, calculated by dividing the total molar ellipticity by the number of amino acids in the molecule.

MCD spectra were recorded by using the GMW Magnet Systems Model 3470 electromagnet, coupled with the Jasco J-815 circular dichroism spectropolarimeter. The cell path length was 1.0 cm. The parameters for the acquisitions were: 1.0 nm bandwidth, 20 nm/min scan rate, 0.2 nm resolution and 9 kG (0.9 T) magnetic field. The magnetic-field direction was set to be parallel to the direction of light propagation. Magnetic-field strength was determined by using a freshly prepared solution of potassium ferricyanide. The baseline-subtracted MCD spectra have been normalized with respect to the path length, concentration and magnetic field strength ($M^{-1} \text{ cm}^{-1} T^{-1}$). Each MCD spectrum was recorded in direct and reverse magnetic-field directions, which were subtracted from each other to eliminate the contribution due to circular dichroism and then divided by two.

The MCD magnitude is thus expressed by the differential molar absorption coefficient, $\Delta\epsilon_M$, in $M^{-1} \text{ cm}^{-1} T^{-1}$, which is related to $[\theta]_M$ ($\text{deg dmol}^{-1} T^{-1}$) by the relationship $[\theta]_M = 3300 \cdot \Delta\epsilon_M$.

Acknowledgements

The authors wish to thank Giuseppina Matarese and Fabrizia Sibillo for technical assistance, Claudia Vicari for helpful discussion, and Luigi Di Costanzo for critically reading the manuscript.

The EU and the Italian MIUR (PON FUZI 2012/2015, CUP B21C12000560005), which supported this work, the STRAIN PROJECT (POR Campania FSE 2007/2013 CUP B25B0900000000), which provided a postdoctoral fellowship to RV, and the Cost action CM1003 are kindly acknowledged.

Notes and references

^a Department of Chemical Sciences, University of Naples “Federico II”, Via Cintia, 80126 Naples, Italy. E-mail: vincenzo.pavone@unina.it, angela.lombardi@unina.it
^b Collège de France, 11 place Marcelin Berthelot, 75231 Paris Cedex 05, France
^c IBB, CNR, Via Mezzocannone 16, 80134 Naples, Italy
^d IMAST Scarl Piazza Bovio 22, 80133 Naples, Italy,

Electronic Supplementary Information (ESI) available: See DOI: 10.1039/b000000x/

- O. Maglio, F. Nastri and A. Lombardi, in *Ionic Interactions in Natural and Synthetic Macromolecules*, eds. A. Ciferri and A. Perico, John Wiley & Sons, Inc., Hoboken, NJ, USA, 2012, pp. 361–450.
- P. A. Sontz, W. J. Song and F. A. Tezcan, *Curr. Opin. Chem. Biol.*, 2014, **19**, 42–49.
- F. Nastri, R. Bruni, O. Maglio and A. Lombardi, in *Coordination Chemistry in Protein Cages*, eds. T. Ueno and Y. Watanabe, John Wiley & Sons, Inc., 2013, pp. 43–85.
- A. J. Reig, M. M. Pires, R. A. Snyder, Y. Wu, H. Jo, D. W. Kulp, S. E. Butch, J. R. Calhoun, T. G. Szyperski, E. I. Solomon and W. F. DeGrado, *Nat. Chem.*, 2012, **4**, 900–906.
- M. L. Zastrow, A. F. A. Peacock, J. A. Stuckey and V. L. Pecoraro, *Nat. Chem.*, 2011, **4**, 118–123.
- F. Yu, V. M. Cangelosi, M. L. Zastrow, M. Tegoni, J. S. Plegaria, A. G. Tebo, C. S. Mocny, L. Ruckthong, H. Qayyum and V. L. Pecoraro, *Chem. Rev.*, 2014, 140324100753004.
- J. Kaplan and W. F. DeGrado, *Proc. Natl. Acad. Sci. U. S. A.*, 2004, **101**, 11566–11570.
- M. Faiella, C. Andreozzi, R. T. M. de Rosales, V. Pavone, O. Maglio, F. Nastri, W. F. DeGrado and A. Lombardi, *Nat Chem Biol*, 2009, **5**, 882–884.
- R. Torres Martin de Rosales, M. Faiella, E. Farquhar, L. Que, C. Andreozzi, V. Pavone, O. Maglio, F. Nastri and A. Lombardi, *JBIC J. Biol. Inorg. Chem.*, 2010, **15**, 717–728.
- F. Nastri, L. Lista, P. Ringhieri, R. Vitale, M. Faiella, C. Andreozzi, P. Travascio, O. Maglio, A. Lombardi and V. Pavone, *Chem. - Eur. J.*, 2011, **17**, 4444–4453.
- M. Faiella, O. Maglio, F. Nastri, A. Lombardi, L. Lista, W. R. Hagen and V. Pavone, *Chem. - Eur. J.*, 2012, **18**, 15960–15971.
- R. L. Koder, J. L. R. Anderson, L. A. Solomon, K. S. Reddy, C. C. Moser and P. L. Dutton, *Nature*, 2009, **458**, 305–309.
- I. D. Petrik, J. Liu and Y. Lu, *Curr. Opin. Chem. Biol.*, 2014, **19**, 67–75.
- M. Dürrenberger and T. R. Ward, *Curr. Opin. Chem. Biol.*, 2014, **19**, 99–106.
- J. L. R. Anderson, C. T. Armstrong, G. Kodali, B. R. Lichtenstein, D. W. Watkins, J. A. Mancini, A. L. Boyle, T. A. Farid, M. P. Crump, C. C. Moser and P. L. Dutton, *Chem. Sci.*, 2014, **5**, 507.
- A. Lombardi, F. Nastri and V. Pavone, *Chem. Rev.*, 2001, **101**, 3165–3190.
- F. Nastri, A. Lombardi, L. D. D’Andrea, M. Sanseverino, O. Maglio and V. Pavone, *Biopolymers*, 1998, **47**, 5–22.
- F. Nastri, A. Lombardi, G. Morelli, O. Maglio, G. D’Auria, C. Pedone and V. Pavone, *Chem. - Eur. J.*, 1997, **3**, 340–349.
- G. D’Auria, O. Maglio, F. Nastri, A. Lombardi, M. Mazzeo, G. Morelli, L. Paolillo, C. Pedone and V. Pavone, *Chem. - Eur. J.*, 1997, **3**, 350–362.
- F. Nastri, A. Lombardi, G. Morelli, C. Pedone, V. Pavone, G. Chottard, P. Battioni and D. Mansuy, *J. Biol. Inorg. Chem.*, 1998, **3**, 671–681.
- A. Lombardi, F. Nastri, M. Sanseverino, O. Maglio, C. Pedone and V. Pavone, *Inorganica Chim. Acta*, 1998, **275-276**, 301–313.
- A. Lombardi, F. Nastri, D. Marasco, O. Maglio, G. De Sanctis, F. Sinibaldi, R. Santucci, M. Coletta and V. Pavone, *Chem. - Eur. J.*, 2003, **9**, 5643–5654.

23. L. Costanzo, S. Geremia, L. Randaccio, F. Nistri, O. Maglio, A. Lombardi and V. Pavone, *JBC J. Biol. Inorg. Chem.*, 2004, **9**, 1017–1027.
24. C. Vicari, I. H. Saraiva, O. Maglio, F. Nistri, V. Pavone, R. O. Louro and A. Lombardi, *Chem. Commun.*, 2014, **50**, 3852.
25. A. Ranieri, S. Monari, M. Sola, M. Borsari, G. Battistuzzi, P. Ringhieri, F. Nistri, V. Pavone and A. Lombardi, *Langmuir*, 2010, **26**, 17831–17835.
26. R. Vitale, L. Lista, S. Lau-Truong, R. T. Tucker, M. J. Brett, B. Limoges, V. Pavone, A. Lombardi and V. Balland, *Chem. Commun.*, 2014, **50**, 1894.
27. W. Humphrey, A. Dalke and K. Schulten, *J. Mol. Graph.*, 1996, **14**, 33–38, 27–28.
28. K. O'Neil and W. DeGrado, *Science*, 1990, **250**, 646–651.
29. Buchler, J.W., in *The Porphyrins*, NY, USA, Academic Press., 1979, vol. I, pp. 389–483.
30. J. N. Rodriguez-Lopez, A. T. Smith and R. N. Thorneley, *J. Biol. Chem.*, 1996, **271**, 4023–4030.
31. H. M. Marques, *Dalton Trans. Camb. Engl.* 2003, 2007, 4371–4385.
32. L. Vickery, T. Nozawa and K. Sauer, *J. Am. Chem. Soc.*, 1976, **98**, 351–357.
33. L. Vickery, T. Nozawa and K. Sauer, *J. Am. Chem. Soc.*, 1976, **98**, 343–350.
34. M. Hatano and T. Nozawa, *Adv. Biophys.*, 1978, **11**, 95–149.
35. T. Nozawa, N. Kobayashi and M. Hatano, *Biochim. Biophys. Acta*, 1976, **427**, 652–662.
36. N. Kobayashi, T. Nozawa and M. Hatano, *Biochim. Biophys. Acta*, 1977, **493**, 340–351.
37. M. Nagai, Y. Nagai, K. Imai and S. Neya, *Chirality*, 2014.
38. G. Blauer, N. Sreerama and R. W. Woody, *Biochemistry (Mosc.)*, 1993, **32**, 6674–6679.
39. M. Kajiyoshi and F. K. Anan, *J. Biochem. (Tokyo)*, 1975, **78**, 1087–1095.
40. F. J. Blanco, G. Rivas and L. Serrano, *Nat. Struct. Biol.*, 1994, **1**, 584–590.
41. A. Jasanoff and A. R. Fersht, *Biochemistry (Mosc.)*, 1994, **33**, 2129–2135.
42. E. R. Main and S. E. Jackson, *Nat. Struct. Biol.*, 1999, **6**, 831–835.
43. D.-P. Hong, M. Hoshino, R. Kuboi and Y. Goto, *J. Am. Chem. Soc.*, 1999, **121**, 8427–8433.
44. H. Reiersen and A. R. Rees, *Protein Eng. Des. Sel.*, 2000, **13**, 739–743.
45. D. Roccatano, G. Colombo, M. Fioroni and A. E. Mark, *Proc. Natl. Acad. Sci.*, 2002, **99**, 12179–12184.
46. T. L. Poulos and J. Kraut, *J. Biol. Chem.*, 1980, **255**, 8199–8205.
47. A. M. Azevedo, V. C. Martins, D. M. F. Prazeres, V. Vojinović, J. M. S. Cabral and L. P. Fonseca, in *Biotechnology Annual Review*, Elsevier, 2003, vol. 9, pp. 199–247.
48. N. C. Veitch, *Phytochemistry*, 2004, **65**, 249–259.
49. S. L. Newmyer and P. R. de Montellano, *J. Biol. Chem.*, 1996, **271**, 14891–14896.
50. M. I. Savenkova, J. M. Kuo and P. R. Ortiz de Montellano, *Biochemistry (Mosc.)*, 1998, **37**, 10828–10836.